High-efficiency magnon-mediated magnetization switching in all-oxide heterostructures with perpendicular magnetic anisotropy

Dongxing Zheng, Jin Lan, Bin Fang, Yan D Li, Chen Liu, J. Omar Ledesma-Martin, Yan Wen, Peng Li, Chenhui Zhang, Yinchang Ma, et al.

▶ **To cite this version:**

Dongxing Zheng, Jin Lan, Bin Fang, Yan D Li, Chen Liu, et al.. High-efficiency magnon-mediated magnetization switching in all-oxide heterostructures with perpendicular magnetic anisotropy. Advanced Materials, 2022, 34 (34), pp.2203038. 10.1002/adma.202203038 . hal-03831725

HAL Id: hal-03831725
https://hal.science/hal-03831725

Submitted on 27 Oct 2022

HAL is a multi-disciplinary open access archive for the deposit and dissemination of scientific research documents, whether they are published or not. The documents may come from teaching and research institutions in France or abroad, or from public or private research centers.

L'archive ouverte pluridisciplinaire **HAL**, est destinée au dépôt et à la diffusion de documents scientifiques de niveau recherche, publiés ou non, émanant des établissements d'enseignement et de recherche français ou étrangers, des laboratoires publics ou privés.

High-efficiency magnon-mediated magnetization switching in all-oxide heterostructures with perpendicular magnetic anisotropy

*Dongxing Zheng#, Jin Lan#, Bin Fang#, Yan Li#, Chen Liu, J. Omar Ledesma-Martin, Yan Wen, Peng Li, Chenhui Zhang, Yinchang Ma, Ziqiang Qiu, Kai Liu, Aurélien Manchon, and Xixiang Zhang**

D.-X. Zheng, J. Lan, B. Fang, and Y. Li contribute equally.

D.-X. Zheng, B. Fang, Y. Li, C. Liu, J. O. Ledesma-Martin, Y. Wen, P. Li, C.-H. Zhang, Y.-C. Ma, Prof. X.-X. Zhang

Physical Science and Engineering Division, King Abdullah University of Science and Technology, Thuwal 23955–6900, Saudi Arabia

Email: xixiang.zhang@kaust.edu.sa

Prof. J. Lan

Tianjin Key Laboratory of Low Dimensional Materials Physics and Processing Technology, Institute of Advanced Materials Physics, School of Science, Tianjin University, Tianjin 300350, China

Prof. Z.-Q. Qiu

Department of Physics, University of California at Berkeley, Berkeley, CA 94720, USA

Prof. K. Liu

Physics Department, Georgetown University, Washington, DC 20057, USA

Prof. A. Manchon

Aix-Marseille Université, CNRS, CINaM, Marseille, France

Keywords: magnon, magnetization switching, perpendicular magnetic anisotropy, oxide heterostructures

Abstract

The search for efficient approaches to realize local switching of magnetic moments in spintronic devices has attracted extensive attention. One of the most promising approaches is the electrical manipulation of magnetization through electron-mediated spin torque. However, the Joule heat generated via electron motion unavoidably causes substantial energy dissipation and potential damage to spintronic devices. Here, all-oxide heterostructures of $SrRuO_3$/NiO/$SrIrO_3$ were epitaxially grown on $SrTiO_3$ single-crystal substrates following the order of the ferromagnetic transition metal oxide $SrRuO_3$ with perpendicular magnetic anisotropy, insulating and antiferromagnetic NiO, and metallic transition metal oxide $SrIrO_3$ with strong spin–orbit coupling. We demonstrate that instead of the electron spin torques, the magnon torques present in the antiferromagnetic NiO layer could directly manipulate the perpendicular magnetization of the ferromagnetic layer. This magnon mechanism may significantly reduce the electron motion–related energy dissipation from electron-mediated spin currents. Interestingly, the threshold current density to generate a sufficient magnon current to manipulate the magnetization was one order of magnitude smaller than that in conventional metallic systems. These findings suggest a route for developing highly efficient all-oxide spintronic devices operated by magnon current.

Introduction

The electrical manipulation of local magnetization in spintronic devices has become one of the most important and extensively studied mechanisms in information technology, such as in logic and magnetic memory devices. [1-4] Several reports achieved electrical switching of magnetization through electron spin torques acting on the magnetization from electron-mediated spin currents in intricately designed devices. [5-7] An electrical spin current can be generated from heavy metals with strong spin–orbit coupling (SOC) or alternatively from topological insulator/Rashba-split systems through the Edelstein effect, when electric charge currents flow in those materials. [6-11] However, due to the limitation of the diffusion length of electrical spins and charge-to-spin current conversion efficiency, the critical electrical current density flowing through the device must be very high to realize magnetization reversal, thereby unavoidably generating substantial Joule heating. [12] Due to the high packing density of devices in integrated circuits, the Joule heating generated in individual tiny devices adds up to substantial energy loss and increases the device temperature, thus deteriorating the device performance. A preferable alternative approach is the use of magnon torques from an antiferromagnetic (AFM) insulator for manipulating the local magnetization, [13-17] in which magnon current is absorbed by ferromangtic layer, consequently the magnon torque will modulate the magnetization of the FM layer.[18-20] When the torque transferred from the magnon current is sufficiently large, the magnetization reverses. Several advantages are evident for achieving magnetization switching using magnon currents. First, because no electron motion is involved in the magnon current, no Joule heating is generated. Second, the diffusion length of a magnon (in micrometers) is much larger than that of an electron spin (in nanometers). [17] Moreover, in contrast to electric spin currents, magnon currents can propagate through insulating magnetic materials. In most studies, an antiferromagnetic insulator was chosen as a magnon current medium, because it has been demonstrated experimentally and theoretically that the unique characteristics of the antiferromagnetic ordering is much more favorable for the

propagation of magnon current than other insulating materials. [10, 21-24] The magnon mediated magnetization switching was first realized in the trilayer of Bi_2Se_3/insulating AFM NiO/ferromagnetic permalloy (Py) with in-plane magnetic anisotropy. [4] In that system, the topological insulator Bi_2Se_3 generated an electrical spin current, which consequently induced a magnon current at the interface between Bi_2Se_3 and NiO. Then, the magnon current propagated through the NiO layer to the ferromagnetic Py layer and the magnon torque manipulated the in-plane magnetization of the Py layer. In contrast to ferromagnetic materials with in-plane magnetic anisotropy, a perpendicularly magnetized ferromagnetic material is preferred in most applications to increase the packing density with reduced device size. [25-27]

In this work, we demonstrate electrical manipulation of the perpendicular magnetization of an $SrRuO_3$ layer using magnon-mediated spin currents in all-oxide heterostructure of $SrRuO_3$/NiO/$SrIrO_3$ (SRO/NiO/SIO) (Figure 1a), with a low critical switching current density of 8.1×10^5 A cm^{-2}, which is one order smaller than the metallic system. Our findings highlight the significance of epitaxy as a powerful tool for achieving high spin–orbit torque efficiency, exploring the underlying mechanisms at the epitaxial interface, and opening up a new pathway for designing next-generation energy-efficient spintronic devices.

Results and discussions

Owing to the closely matched lattice parameters of SRO, NiO, and SIO, high-quality epitaxial growth of all-oxide SRO/NiO/SIO heterostructures was achieved on (001)-oriented $SrTiO_3$ (STO) substrates using pulsed laser deposition. We chose SIO based on theoretical predictions of strong spin–orbit coupling capable of generating an intrinsic spin Hall effect.[28-32] The spin Hall conductivity of SIO is reported to be in the range of 0.4~1.1,[28, 31-34] which is much larger than that of Pt. Ever since NiO was first shown to be an excellent magnon host, it has been widely used as an intermediate insulating antiferromagnetic layer.[4, 18, 21, 22, 35-39] Further, perpendicular magnetic anisotropy (PMA) can be obtained in the ferromagnetic SRO layer by carefully tuning the layer's thickness and the oxygen pressure during layer

deposition.[29, 40-43] Therefore, in an SRO/NiO/SIO heterostructure, a spin current will be generated by an electric current flowing in the SIO layer through the spin Hall effect, thereby inducing a magnon current in the NiO layer. Finally, the induced magnon current will switch the magnetization in the SRO layer via magnon torque, as schematically shown in Figure 1b.

By carefully optimizing the parameters such as substrate temperature and deposition rate, high-quality SRO(4.8 nm)/NiO(t)/SIO(40 nm) heterostructures with NiO thicknesses (t) varying from 0 to 19.2 nm were epitaxially grown on (001)-oriented STO substrates using pulsed laser deposition system, as shown in Figure 2a (see Supporting Information for growth details). Notably, the high quality of the epitaxial NiO layer is crucial for the propagation of magnons with a well-defined polarization direction and a long spin diffusion length. [37, 44] Because the physical properties of SRO are extremely sensitive to strain (Figure S2) [45], the SRO layer was first grown on TiO_2-teminated STO (001) substrates to ensure PMA in the magnetic layer (Figure 2a). Subsequently, the NiO and SIO layers were deposited. Figure 2b shows the X-ray diffraction θ–2θ pattern obtained for the SRO/NiO(19.2 nm)/SIO heterostructure. The NiO's (002) diffraction peak along with satellite peaks can be observed, indicating good uniformity and crystallinity of the NiO layer. The (00l) diffraction peaks of the SRO and SIO almost overlap with the (00l) diffraction peak of the STO substrate. This is due to the larger lattice parameter of NiO layer, which applies a tensile strain on the SIO layer and leads to the shift of SIO (00l) diffraction peaks towards the STO (00l) diffraction peaks (Figure S3). The good crystallinity and epitaxial growth of the heterostructure were further confirmed by high-resolution cross sectional scanning transmission electron microscopy (STEM) images. Distinct interfaces between STO, SRO, NiO, and SIO layers with continuous lattice fringes are clearly seen (Figures 2c&d). Moreover, the obtained elemental mappings for each layer indicated high-quality growth and distinct interfaces without elemental diffusion across layers (Figure S5).

To shed light on the underlying mechanism in the magnon-mediated spin–orbit torque (SOT) switching of magnetization, the magnetic properties of the samples must first be understood. Therefore, we performed temperature- and magnetic field-dependent magnetization measurements of the samples. Figure 2e shows the out-of-plane *M–H* loops of the SRO/NiO(*t*)/SIO heterostructures with NiO thicknesses (t = 0, 7.2, and 19.2 nm) after cooling the samples from 300 to 10 K under zero external magnetic field. The shapes of the *M–H* loops of the heterostructures indicate the existence of the dominating out-of-plane–magnetic anisotropy in the SRO layer. Besides the slight differences in the coercive field, all the samples showed the same saturation magnetization of approximately 200 emu/cm^3, suggesting that the quality/crystallinity of the SRO layer remained unaffected by the insertion of NiO layer. Figure 2f shows the temperature-dependent magnetization of the SRO/NiO(*t*)/SIO heterostructures. All the *M–T* curves were recorded as the temperature was increased from 10 to 220 K in zero external magnetic field, after the samples were cooled from 300 to 10 K with an out-of-plane magnetic field of 2 T. With increasing temperature, the magnetization decreased monotonically and approached zero at certain temperatures that can be considered Curie temperatures (T_c). These Curie temperatures fall in the range of 105–125 K, below the bulk T_c of 160 K. [46] This reduced T_c is due to the ultrathin SRO layer and the strain from the STO substrates.[45] To gain a deeper understanding of the magnetic anisotropies of these films, we performed *M–T* measurements by applying the magnetic field in each of three directions with the same procedure used for obtaining the *M–T* curves shown in Figure 2f. The *M–T* curves measured for the SRO/NiO(7.2 nm)/SIO heterostructure with the applied magnetic fields oriented along the *x*-, *y*-, or *z*-axis are shown in the inset of Figure 2f. The behaviors of all three curves unambiguously demonstrate the existence of a nearly perfect PMA in the SRO/NiO(7.2 nm)/SIO heterostructure. This finding is consistent with the measurements of angle-dependent magnetoresistance taken by rotating an external magnetic field in the *xy*, *yz*, and *xz* planes (see Figure S8).

Further, to study the magnon-mediated SOT, we performed second-harmonic measurements of the anomalous and planar Hall resistance at 60 K on the SRO/NiO(*t*)/SIO heterostructures-based devices. [4, 47, 48] The schematic of the device geometry is shown in Figure 3a. By applying an alternating current (AC) to the device, an oscillation of magnetization was induced by the alternating SOT, giving rise to a second-harmonic Hall voltage. Due to the PMA of the SRO layer, in-plane magnetic fields that are larger than the PMA effective field H_k of 4 T (see Figure S9) were applied to align the magnetic moment in the *xy* plane during the measurement of the damping-like torque. By rotating the magnetic field in the *xy* plane, the first and second-harmonic Hall resistances were measured as functions of angle φ (Figure 3a). Theoretically, the first and second-harmonic Hall resistances have the following angular dependences:[47-50]

$$R_H^{\omega}=R_P \sin 2\varphi, \tag{1}$$

$$R_H^{2\omega}=R_{FL}^{2\omega} \cos 2\varphi \sin \varphi + (R_{DL}^{2\omega} + R_{SSE}^{2\omega}) \sin \varphi, \tag{2}$$

where R_P is the planar Hall resistance, $R_{SSE}^{2\omega}$ is the spin–Seebeck resistance, and $R_{FL}^{2\omega}$ and $R_{DL}^{2\omega}$ are the field- and damping-like resistances, respectively. In other words, $R_{DL}^{2\omega}=H_{DL}R_H/2(H_{ext}-H_k)$ correlates with the damping-like torque τ_{DL}, where H_{DL} is the effective field induced by the damping-like torque, R_H is the Hall resistance, H_{ext} is the in-plane external magnetic field. The Hall resistance as a function of the out-of-plane magnetic field H_z is plotted in Figure 3b. The first-order harmonic resistance R_H^{ω} as a function of φ measured at H_{ext}=9 T is shown in Figure 3c. Eq. (1) describes the R_H^{ω} data, indicating that the magnetization direction of the SRO layer always follows the direction of the strong external magnetic field. Furthermore, $R_H^{2\omega}$ as a function of φ measured at the same H_{ext} (Figure 3d) is described by Eq. (2). To clearly present the contributions of the damping- and field-like torques to the total SOT, we plotted them in Figure 3d. The contribution of the damping-like torque ($\sin\varphi$, cyan dashed

line) is much larger than that of the field-like torque ($\sin\varphi\cos 2\varphi$, blue solid line), indicating that the damping-like SOT plays a dominant role. Indeed, in Eq. (2), the $\sin\varphi$ term includes the damping-like torque resistances $R_{DL}^{2\omega}$ and the spin–Seebeck resistances $R_{SSE}^{2\omega}$. However, since the spin–Seebeck resistances are independent of the magnetic field,[50, 51] the slope of a linear fit of $R_{\mathrm{DL}}^{2\omega}$ as a function of $1/(H_{\mathrm{ext}} - H_{\mathrm{k}})$ gives information about H_{DL} and the intercepts denote the spin–Seebeck resistances.

Figure 3e shows the experimental data for $R_{\mathrm{DL}}^{2\omega}$ as a function of $1/(H_{\mathrm{ext}} - H_{\mathrm{k}})$ and the linear fits for various SRO/NiO(t)/SIO heterostructures. We then calculated the damping-like torque efficiency $\eta = \Delta H_{\mathrm{DL}}/J_{\mathrm{e}}$ using the data extracted from Figure 3e and plotted it in Figure 3f. The torque efficiency η of the SRO/SIO heterostructure (t = 0 in SRO/NiO(t)/SIO) fabricated on an STO (001) substrate reached 193.1×10^{-6} OeA^{-1}cm^2; which is of the same magnitude as the record-high value of 408.6×10^{-6} OeA^{-1}cm^2 for an SIO/SRO heterostructure fabricated on an STO (110) substrate. [29] For SRO/NiO(t)/SIO heterostructures, as the thickness of the NiO layer increased, the efficiency η increased to 292.5×10^{-6} OeA^{-1}cm^2 and then decreased monotonically. This enhanced η may be attributed to the enhanced spin fluctuation of the thin NiO layer at sub-60-K Néel temperature (see Fig. S15). Several studies have reported that this enhanced spin fluctuation increases the transmission of spin currents. [18, 21, 22, 35] Here, the epitaxial NiO layer with thickness lower than 4.8 nm was found to be discontinuous (see Fig. S4). In this case, there may be a mix of torque current carried by tunneling electrons, magnon, and diffusive electrons in the system acting on the FM layer, which is not an ideal system to study the magnon-mediated magnetization switching. When the NiO layer thickness increased to 7.2 nm, the NiO layer is completely continuous and flat (Fig. 2e), which is suitable for the study of pure magnon-mediated magnetization switching. Although the efficiency η decreased to 51.8×10^{-6} OeA^{-1}cm^2 when the NiO thickness was increased to 7.2 nm, this value is still comparable to or even larger than those found in typical Pt/Co/AlO$_x$ [52, 53] and Ta/CoFeB/MgO

[54] structures. The obtained results highlight the remarkable enhancement of the SOT efficiency in the high-quality epitaxial heterostructures with chemically sharp interfaces. Although the efficiency η was reduced by inserting a thick NiO layer, it was still high in comparison to those in conventional metallic systems. Moreover, the thick NiO layer completely blocked the vertical motion of electrons, effectively reducing Joule heating, thus improving device stability.

Next, we demonstrate that the large damping-like SOT observed in these heterostructures can be employed to switch the magnetization of the SRO layer. The left and right panels in Figure 4a show schematics of SOT-driven magnetization switching and an optical image of the corresponding device, respectively. The magnetization switching driven by spin current generated in the SIO layer was realized in the SRO/SIO bilayer with the assistance of an in-plane magnetic field that was applied along the electric current direction. As shown in Figure 4b, when an opposite in-plane magnetic field was applied, the switching polarity reversed, further confirming that the magnetization switching was driven solely by SOT. When an insulating and antiferromagnetic NiO layer with thickness 7.2 nm was inserted between the SRO and SIO layers, the spin-current flow carried by electron transport from the SIO layer to SRO layer was blocked. However, magnons were excited in the NiO layer by the spin current generated in the SIO layer, which consequently propagated to the SRO layer. The spin angular momenta of the electronic spin current were thus transferred to the magnetization through the magnon current, enabling the magnetization switching in the SRO layer. Figure 4c shows magnetization switching behavior mediated by magnons in the SRO/NiO/SIO trilayer system. Notably, the magnetization polarity reversed when an in-plane magnetic field was applied in the opposite direction, thus behaving in the same way as magnetization switching induced by SOT from the electronic spin current generated from SIO layer in the SRO/SIO bilayer (Figure 4b). Comparing the results in Figure 4c with the AHE loop in Figure 3b, it is found that the change of R_H induced by the electrical current was about 22% of the total anomalous R_H change. This is mainly induced by the Joule heating during the SOT switching measurement, which

leads to a temperature rise of 21 K (see Fig. S6). The temperature rise would lead to a reduced magnetization and hence an incomplete SOT switching (see discussion in Figure S12), which was also observed in the previous studies.[29, 55]

Figures 4d&e show the magnetization switching represented by $\Delta R_H/\Delta R_H(\max)$ plotted as functions of the magnetic field and electric current for the bilayer SRO/SIO and trilayer SRO/NiO/SIO, respectively. Here, ΔR_H is defined as $\Delta R_H=R-R_{min}$, $\Delta R_H(\max)$ is defined as $\Delta R_H(\max)=R_{max}-R_{min}$ in each *R-J* loop at different magnetic fields. The zero, partial, and full-switching states of the magnetization that that can be switched by electrical current in the SRO layer under the interplay of the SOT and in-plane magnetic field are shown in blue, green, and red, respectively. As indicated by the orange dashed lines, the critical switching current density (J_C) values of the SRO/SIO bilayer and the SRO/NiO/SIO trilayer decreased quasi-linearly with increasing H_x. This behavior is consistent with that observed in systems with PMA, but there the magnetization switching was manipulated by the spin Hall effect.[56, 57] Moreover, the J_C in the SRO/NiO(7.2 nm)/SIO trilayer were as low as 8.1×10^5 A cm^{-2} at 1600 Oe. These J_C values are one order of magnitude smaller than that required in normal metallic systems, [5, 53, 54] which can be primarily ascribed to the following factors. It has been reported that the critical switching current is proportional to the saturation magnetization M_s of the ferromagnetic layer and inversely proportional to the magnon mediated charge to spin conversion efficiency θ.[56] The value of θ can be expressed as $\theta=\kappa T_{int}\theta_{SIO}$, where κ is the magnon related spin transport efficiency, T_{int} is the interfacial spin transparency, θ_{SIO} is the spin Hall angle of the SIO layer. [39] As the J_c is proportional to the saturation magnetization M_s, thus the relatively small M_s in the SRO layer contributes to the low J_c observed in this study. In addition to the low *M*s, the contribution from the large θ should also play an important role. The large θ may be associated with three factors in this study. The first is the large spin Hall angle of the epitaxial SIO layer, which is reported to be in the range of 0.4~1.1.[31-33] The second is the large spin

transparency T_{int} of the epitaxial interface. Since T_{int} is mainly dominated by the spin back flow and spin memory loss at the interface[58-60], the high-quality interface which can suppress the spin back flow and spin memory loss should favor a large T_{int}. For example, Huang *et al.* had reported that the atomically sharp interface between ferromagnetic $La_{0.7}Sr_{0.3}MnO_3$ and metallic SIO layers exhibited a highly efficient charge-to-spin conversion.[32]

In addition, we also studied magnetization switching in samples with various SIO layer thicknesses. In particular, we noticed that although the J_C value increased rapidly with decreasing SIO layer thickness, the critical switching current I_C seemed to be independent of the thickness (Figure S13). This observation may indicate that the magnetization switching in SRO layer requires a critical torque current and that the SIO layer has a long spin diffusion length in the all-oxide epitaxial heterostructures.

Conclusion

In Summary, the magnon-mediated magnetization switching was realized in an all-oxide SRO/NiO/SIO heterostructure with PMA. We demonstrated that the magnon current excited in the insulating antiferromagnetic layer by electronic spin current was effective to manipulate the perpendicular magnetization in a ferromagnetic layer. Furthermore, the critical electric current to enable magnetization switching was 9×10^5 A cm^{-2}, about one order of magnitude smaller than in conventional metallic systems. Based on these findings, the epitaxial oxide heterostructure is found to have a unique advantage over conventional metallic systems and metal/topological insulator systems. The epitaxial oxide heterostructure is not only good conductor as a metallic system, but also has a high spin–orbit torque efficiency, comparable to that of metal/topological insulator systems. Moreover, the all-oxide heterostructures can be prepared in a single synthesis step, unlike systems including two-dimensional materials and/or topological insulators that require an additional transfer process or separate preparations. These findings suggest that the all-oxide epitaxial heterostructure is a promising candidate for

realizing effective magnon-mediated magnetization switching, which opens up a new pathway for designing next-generation energy-efficient spintronic devices.

Experimental Section

Sample preparation. A series of $SrRuO_3$/NiO(t)/$SrIrO_3$ (SRO/NiO(t)/SIO) heterostructures (t = thickness) were grown on 0.5-mm-thick TiO_2-terminated (001)-oriented $SrTiO_3$ (STO) substrates (10 mm $\times$ 10 mm) using the pulsed laser deposition method. The STO substrates were first placed in boiling water for 10 min and then, annealed in a tube furnace at 1000 °C with an oxygen partial pressure of 60 Torr for 6 hours. After the annealing process, the TiO_2-terminated (001)-oriented STO substrates were then ready for growth of samples. The high quality of the surface of the substrates was confirmed through surface morphology measurements using atomic force microscopy. During deposition, the SRO, SIO, and STO targets were ablated by a KrF excimer laser (wavelength = 248 nm) at a repetition rate of 3 Hz and a fluence of 1.35 J/cm^2. The substrate temperature was kept at 800 °C, and the oxygen partial pressure was maintained at 8 Pa. After the deposition, samples were annealed *in situ* for 30 min at 800 °C and an oxygen pressure of 1 Torr. Finally, the samples were passively cooled to room temperature (with the cooling rate of approximately 20 °C/min) and kept at the same oxygen pressure of 1 Torr.

Scanning transmission electron microscopy characterization. Monochromated Cs-corrected high-resolution scanning transmission electron microscopy (STEM; Titan 80-300, FEI) investigations were performed to characterize the interfaces and structure of the samples. The samples for STEM experiments were prepared using a focused ion beam (FIB; Helios 450, FEI).

Electrical transport and magnetic properties characterization. The electron beam lithography technique (JEOL e-beam writer), the ma-N 2403 (micro resist technology GmbH) photoresist, and Ar ion etcher have been used in the first step to fabricate the Hall bar. Then the laser writer was used to write the pattern of the electrode. Finally, the Ti/Au electrode with the Ti thickness of 10 nm and Au thickness of 100 nm was deposited. The anomalous Hall effect, harmonic Hall resistance, and current-induced magnetization switching were measured on Hall

bar devices (Figure 4a). The electrical transport properties were measured using a Quantum Design Physical Property Measurement System. The magnetic properties were measured using a Quantum Design Magnetic Properties Measurement System. The first and second harmonic Hall resistances (voltages) were measured using two Stanford SR830 lock-in amplifiers. The Keithley 6221 source meter was used to apply an alternating current (AC) with a frequency of 72.9 Hz. The Keithley 6221 source meter was also used to apply the pulse current. The Keithley 2182 voltage meter was used to measure the Hall voltage.

Supporting Information

Supporting Information is available from the Wiley Online Library or from the author.

Acknowledgments

This publication is based on research supported by the King Abdullah University of Science and Technology, Office of Sponsored Research (OSR), under award No. OSR-2017-CRG6-3427 and OSR-2019-CRG8-4081. D.X.Z. acknowledges financial support from the National Natural Science Foundation of China (11704278) and the Natural Science Foundation of Tianjin City (19JCQNJC03000). Z.Q.Q acknowledges financial support of US Department of Energy, Office of Science, Office of Basic Energy Sciences, Materials Sciences and Engineering Division under Contract No. DE-AC02-05-CH11231 (van der Waals heterostructures program, KCWF16). K.L. acknowledges support from the US NSF (DMR-2005108).

Received: ((will be filled in by the editorial staff))
Revised: ((will be filled in by the editorial staff))
Published online: ((will be filled in by the editorial staff))

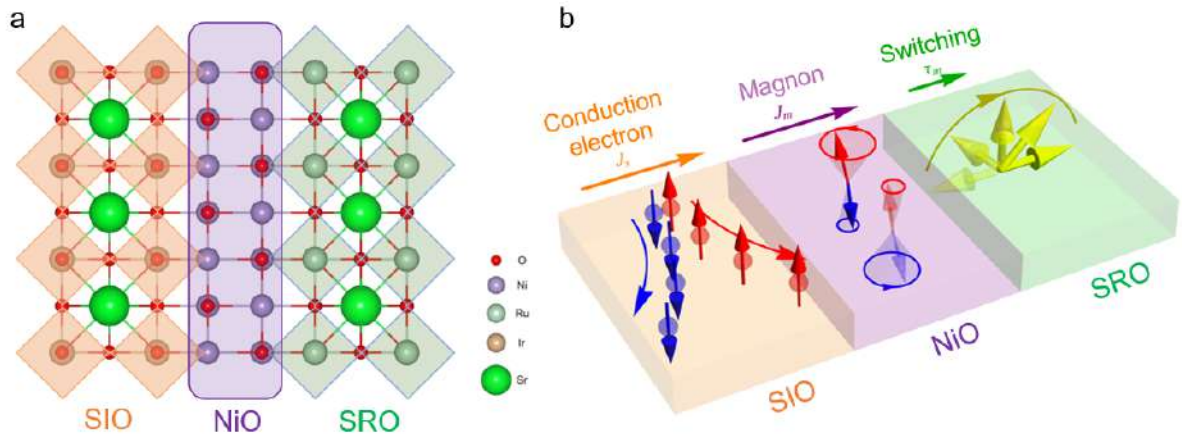

Figure 1. Schematics of the SRO/NiO/SIO heterostructure and magnon-mediated magnetization switching. a) Atomic structure of the SRO/NiO/SIO heterostructure. b) Magnon-mediated magnetization switching in the SRO/NiO/SIO heterostructures.

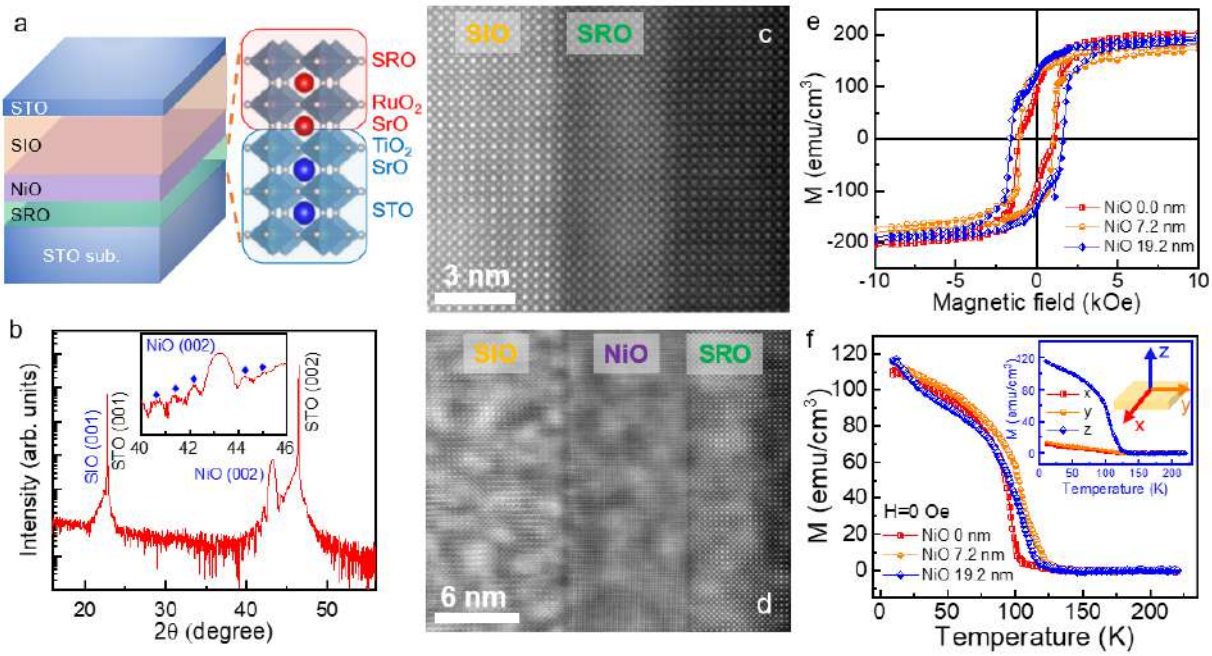

Figure 2. Structural and magnetic characterization of the SRO/NiO/SIO heterostructures. a) Schematic of the SRO/NiO(*t*)/SIO heterostructures and layer-growth sequence on TiO_2-terminated STO substrates. b) θ–2θ X-ray diffraction pattern of SRO/NiO(19.2 nm)/SIO heterostructure. The inset shows an enlarged view of the NiO (002) diffraction peak. Cross-sectional scanning transmission electron microscopy images of the (c) SRO/SIO bilayer and (d) SRO/NiO (7.2 nm)/SIO trilayer grown on the STO substrates. e) *M*–*H* loops of the SRO/NiO(*t*)/SIO heterostructures with different thicknesses at 60 K. f) Temperature-dependent magnetization of the SRO/NiO(*t*)/SIO heterostructures. For each *M*–*T* curve, the samples were field-cooled from 300 to 10 K in the presence of an out-of-plane magnetic field of 2 T. The magnetization was then measured by increasing the temperature in the absence of external magnetic field. The inset shows the *M*–*T* curves of an SRO/NiO(7.2 nm)/SIO heterostructure measured under the same conditions with the sample cooled along the *x*-, *y*-, and *z*-directions, as illustrated in the schematic.

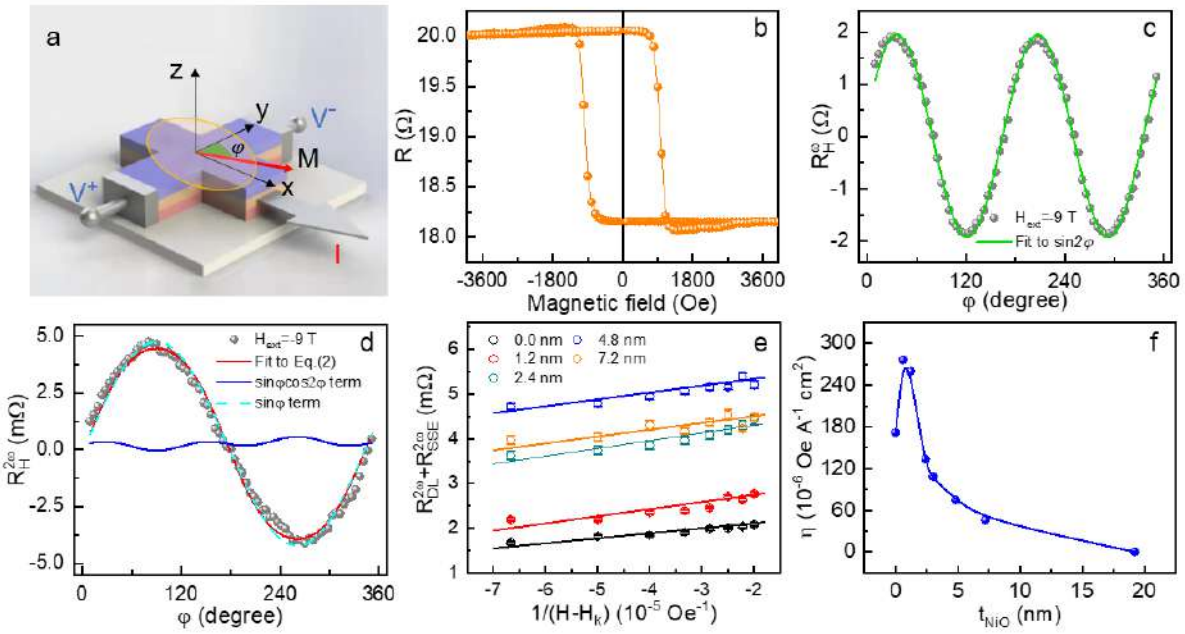

Figure 3. Spin transport and SOT measurement of the SRO/NiO(*t*)/SIO heterostructures. a) Schematic of the experimental setup used for harmonic Hall voltage measurements. b) Hall resistance in the SRO/NiO(7.2 nm)/SIO heterostructure as measured in the presence of an out-of-plane magnetic field at 60 K. The AHE loop is offset horizontally. c) Planar Hall resistance in the SRO/NiO(7.2 nm)/SIO heterostructure as a function of the rotation angle φ with an in-plane magnetic field of −9 T and temperature at 60 K. d) Second-harmonic Hall resistance in the SRO/NiO(7.2 nm)/SIO heterostructure as a function of φ with an in-plane magnetic field of −9 T and temperature at 60 K. The red solid line is the fitting to Eq. (2). Both $\sin\varphi\cos 2\varphi$ (dashed cyan line) and $\sin\varphi$ (solid blue line) are also plotted here. e) Summary of $R_{\mathrm{DL}}^{2\omega}$ and $R_{\mathrm{SSE}}^{2\omega}$ as functions of the external magnetic field for the SRO/NiO(*t*)/SIO heterostructures, where H_k is the anisotropy field of approximately 4 T. f) NiO thickness-dependent efficiency of damping-like torque $\Delta H_{\mathrm{DL}}/J_{\mathrm{e}}$.

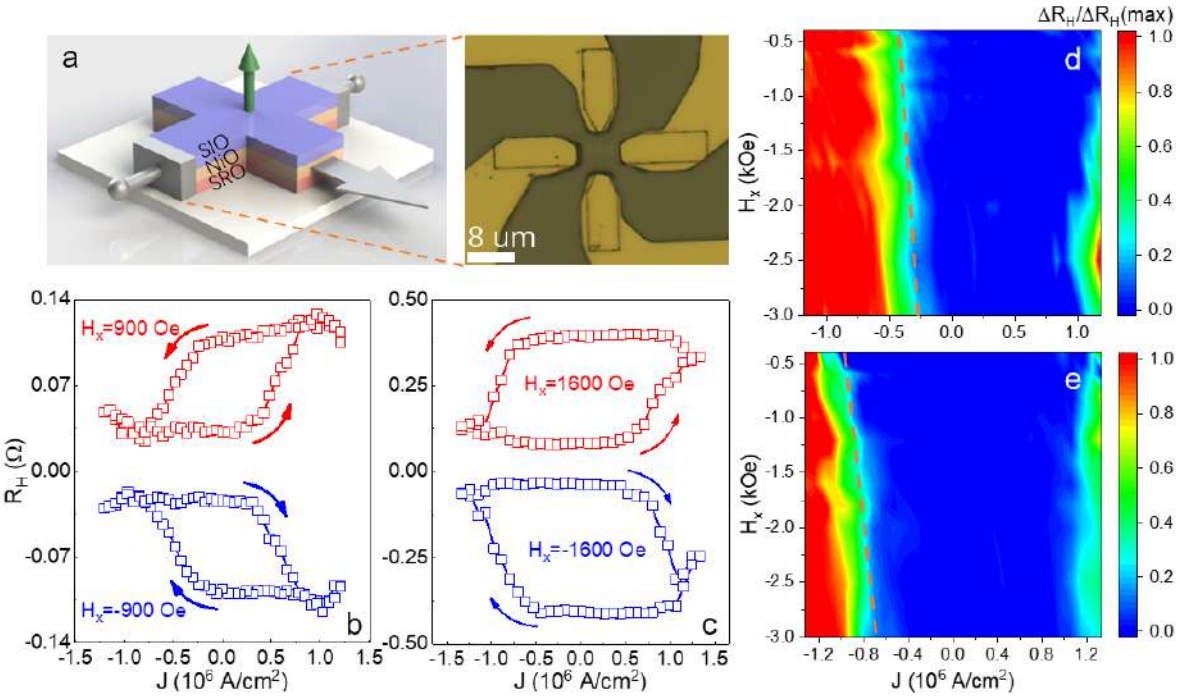

Figure 4. Magnon-mediated magnetization switching in the SRO/NiO(*t*)/SIO heterostructures. a) Schematic of the setup for magnon-mediated magnetization switching measurements. The right panel shows optical microscopy image of the device. b) Electronic spin current–induced magnetization switching in SRO/SIO heterostructures at 60 K. c) Magnon-mediated magnetization switching in the SRO/NiO(7.2 nm)/SIO heterostructure at 60 K. d) Spin current and (e) phase diagram of magnon-mediated magnetization switching as functions of the applied current and magnetic field, which is constructed from the measurements shown in (b) and (c) under various magnetic fields H_x.

References

[1] A. Chen, Y. Wen, B. Fang, Y. Zhao, Q. Zhang, Y. Chang, P. Li, H. Wu, H. Huang, Y. Lu, Z. Zeng, J. Cai, X. Han, T. Wu, X. X. Zhang, Y. Zhao, *Nat. Commun.* **2019**, 10, 243.
[2] A. Chen, Y. Zhao, Y. Wen, L. Pan, P. Li, X.-X. Zhang, *Sci. Adv.* **2019**, 5, eaay5141.
[3] W.-G. Wang, M. Li, S. Hageman, C. Chien, *Nat. Mater.* **2012**, 11, 64.
[4] Y. Wang, D. Zhu, Y. Yang, K. Lee, R. Mishra, G. Go, S.-H. Oh, D.-H. Kim, K. Cai, E. J. S. Liu, *Science* **2019**, 366, 1125.
[5] I. M. Miron, K. Garello, G. Gaudin, P. J. Zermatten, M. V. Costache, S. Auffret, S. Bandiera, B. Rodmacq, A. Schuhl, P. Gambardella, *Nature* **2011**, 476, 189.
[6] L. Liu, O. J. Lee, T. J. Gudmundsen, D. C. Ralph, R. A. Buhrman, *Phys. Rev. Lett.* **2012**, 109, 096602.

[7] L. Liu, C.-F. Pai, Y. Li, H. Tseng, D. Ralph, R. Buhrman, *Science* **2012**, 336, 555.
[8] A. R. Mellnik, J. S. Lee, A. Richardella, J. L. Grab, P. J. Mintun, M. H. Fischer, A. Vaezi, A. Manchon, E. A. Kim, N. Samarth, D. C. Ralph, *Nature* **2014**, 511, 449.
[9] Y. Shiomi, K. Nomura, Y. Kajiwara, K. Eto, M. Novak, K. Segawa, Y. Ando, E. Saitoh, *Phys. Rev. Lett.* **2014**, 113, 196601.
[10] A. Manchon, J. Železný, I. M. Miron, T. Jungwirth, J. Sinova, A. Thiaville, K. Garello, P. Gambardella, *Rev. Mod. Phys.* **2019**, 91, 035004.
[11] J. C. Rojas-Sanchez, S. Oyarzun, Y. Fu, A. Marty, C. Vergnaud, S. Gambarelli, L. Vila, M. Jamet, Y. Ohtsubo, A. Taleb-Ibrahimi, P. Le Fevre, F. Bertran, N. Reyren, J. M. George, A. Fert, *Phys. Rev. Lett.* **2016**, 116, 096602.
[12] M. Zwierzycki, Y. Tserkovnyak, P. J. Kelly, A. Brataas, G. E. Bauer, *Phys. Rev. B* **2005**, 71, 064420.
[13] V. V. Kruglyak, S. O. Demokritov, D. Grundler, *J. Phys. D: Appl. Phys.* **2010**, 43.
[14] A. Khitun, M. Bao, K. L. Wang, *J. Phys. D: Appl. Phys.* **2010**, 43.
[15] Y. Kajiwara, K. Harii, S. Takahashi, J. Ohe, K. Uchida, M. Mizuguchi, H. Umezawa, H. Kawai, K. Ando, K. Takanashi, S. Maekawa, E. Saitoh, *Nature* **2010**, 464, 262.
[16] A. V. Chumak, V. I. Vasyuchka, A. A. Serga, B. Hillebrands, *Nat. Phys.* **2015**, 11, 453.
[17] R. Lebrun, A. Ross, S. A. Bender, A. Qaiumzadeh, L. Baldrati, J. Cramer, A. Brataas, R. A. Duine, M. Klaui, *Nature* **2018**, 561, 222.
[18] H. Wang, J. Finley, P. Zhang, J. Han, J. T. Hou, L. Liu, *Phys. Rev. Appl.* **2019**, 11, 044070.
[19] C. Y. Guo, C. H. Wan, M. K. Zhao, C. Fang, T. Y. Ma, X. Wang, Z. R. Yan, W. Q. He, Y. W. Xing, J. F. Feng, X. F. Han, *Phys. Rev. B* **2021**, 104, 094412.
[20] X. Zhao, S. Mao, H. Wang, D. Wei, J. Zhao, *Appl. Phys. Lett.* **2021**, 118, 092401.
[21] H. Wang, C. Du, P. C. Hammel, F. Yang, *Phys. Rev. Lett.* **2014**, 113, 097202.
[22] W. Lin, K. Chen, S. Zhang, C. L. Chien, *Phys. Rev. Lett.* **2016**, 116, 186601.
[23] Y. Wen, F. Zhuo, Y. Zhao, P. Li, Q. Zhang, A. Manchon, X.-x. Zhang, *Phys. Rev. Appl.* **2019**, 12, 054030.
[24] S. M. Rezende, R. L. Rodríguez-Suárez, A. Azevedo, *Phys. Rev. B* **2016**, 93, 054412.
[25] N. Nishimura, T. Hirai, A. Koganei, T. Ikeda, K. Okano, Y. Sekiguchi, Y. Osada, *J. Appl. Phys.* **2002**, 91, 5246.
[26] S. Emori, U. Bauer, S.-M. Ahn, E. Martinez, G. S. Beach, *Nat. Mater.* **2013**, 12, 611.
[27] S. Mangin, D. Ravelosona, J. Katine, M. Carey, B. Terris, E. E. Fullerton, *Nat. Mater.* **2006**, 5, 210.
[28] A. S. Patri, K. Hwang, H.-W. Lee, Y. B. Kim, *Sci. Rep.* **2018**, 8, 8052.
[29] L. Liu, Q. Qin, W. Lin, C. Li, Q. Xie, S. He, X. Shu, C. Zhou, Z. Lim, J. Yu, W. Lu, M. Li, X. Yan, S. J. Pennycook, J. Chen, *Nat. Nanotechnol.* **2019**, 14, 939.
[30] Y. Kozuka, S. Isogami, K. Masuda, Y. Miura, S. Das, J. Fujioka, T. Ohkubo, S. Kasai, *Phys. Rev. Lett.* **2021**, 126, 236801.
[31] T. Nan, T. J. Anderson, J. Gibbons, K. Hwang, N. Campbell, H. Zhou, Y. Q. Dong, G. Y. Kim, D. F. Shao, T. R. Paudel, N. Reynolds, X. J. Wang, N. X. Sun, E. Y. Tsymbal, S. Y. Choi, M. S. Rzchowski, Y. B. Kim, D. C. Ralph, C. B. Eom, *Proc Natl Acad Sci U S A* **2019**, 116, 16186.
[32] X. Huang, S. Sayed, J. Mittelstaedt, S. Susarla, S. Karimeddiny, L. Caretta, H. Zhang, V. A. Stoica, T. Gosavi, F. Mahfouzi, Q. Sun, P. Ercius, N. Kioussis, S. Salahuddin, D. C. Ralph, R. Ramesh, *Adv. Mater.* **2021**, 33, e2008269.
[33] H. Wang, K.-Y. Meng, P. Zhang, J. T. Hou, J. Finley, J. Han, F. Yang, L. Liu, *Appl. Phys. Lett.* **2019**, 114.
[34] G.-Y. Guo, S. Murakami, T.-W. Chen, N. Nagaosa, *Phys. Rev. Lett.* **2008**, 100, 096401.

[35] W. Lin, C. L. Chien, *Phys. Rev. Lett.* **2017**, 118, 067202.
[36] D. Hou, Z. Qiu, J. Barker, K. Sato, K. Yamamoto, S. Velez, J. M. Gomez-Perez, L. E. Hueso, F. Casanova, E. Saitoh, *Phys. Rev. Lett.* **2017**, 118, 147202.
[37] B.-W. Dong, L. Baldrati, C. Schneider, T. Niizeki, R. Ramos, A. Ross, J. Cramer, E. Saitoh, M. Kläui, *Appl. Phys. Lett.* **2019**, 114, 102405.
[38] C. Hahn, G. de Loubens, V. V. Naletov, J. Ben Youssef, O. Klein, M. Viret, *EPL (Europhysics Letters)* **2014**, 108, 57005.
[39] L. Zhu, L. Zhu, R. A. Buhrman, *Phys. Rev. Lett.* **2021**, 126, 107204.
[40] W. Lu, P. Yang, W. D. Song, G. M. Chow, J. S. Chen, *Phys. Rev. B* **2013**, 88, 214115.
[41] A. F. Marshall, L. Klein, J. S. Dodge, C. H. Ahn, J. W. Reiner, L. Mieville, L. Antagonazza, A. Kapitulnik, T. H. Geballe, M. R. Beasley, *J. Appl. Phys.* **1999**, 85, 4131.
[42] D. Zheng, Y. W. Fang, S. Zhang, P. Li, Y. Wen, B. Fang, X. He, Y. Li, C. Zhang, W. Tong, W. Mi, H. Bai, H. N. Alshareef, Z. Q. Qiu, X. Zhang, *ACS Nano* **2021**, 15, 5086.
[43] C. U. Jung, H. Yamada, M. Kawasaki, Y. Tokura, *Appl. Phys. Lett.* **2004**, 84, 2590.
[44] M. Dabrowski, T. Nakano, D. M. Burn, A. Frisk, D. G. Newman, C. Klewe, Q. Li, M. Yang, P. Shafer, E. Arenholz, T. Hesjedal, G. van der Laan, Z. Q. Qiu, R. J. Hicken, *Phys. Rev. Lett.* **2020**, 124, 217201.
[45] G. Koster, L. Klein, W. Siemons, G. Rijnders, J. S. Dodge, C.-B. Eom, D. H. A. Blank, M. R. Beasley, *Rev. Mod. Phys.* **2012**, 84, 253.
[46] A. Kanbayasi, *J. Phys. Soc. Jpn.* **1976**, 41, 1876.
[47] Q. Shao, C. Tang, G. Yu, A. Navabi, H. Wu, C. He, J. Li, P. Upadhyaya, P. Zhang, S. A. Razavi, Q. L. He, Y. Liu, P. Yang, S. K. Kim, C. Zheng, Y. Liu, L. Pan, R. K. Lake, X. Han, Y. Tserkovnyak, J. Shi, K. L. Wang, *Nat. Commun.* **2018**, 9, 3612.
[48] Y. Wen, J. Wu, P. Li, Q. Zhang, Y. Zhao, A. Manchon, J. Q. Xiao, X. Zhang, *Phys. Rev. B* **2017**, 95, 104403.
[49] Q. Shao, G. Yu, Y. W. Lan, Y. Shi, M. Y. Li, C. Zheng, X. Zhu, L. J. Li, P. K. Amiri, K. L. Wang, *Nano Lett.* **2016**, 16, 7514.
[50] C. O. Avci, K. Garello, M. Gabureac, A. Ghosh, A. Fuhrer, S. F. Alvarado, P. Gambardella, *Phys. Rev. B* **2014**, 90, 224427.
[51] K.-i. Uchida, H. Adachi, T. Ota, H. Nakayama, S. Maekawa, E. Saitoh, *Appl. Phys. Lett.* **2010**, 97, 172505.
[52] I. M. Miron, G. Gaudin, S. Auffret, B. Rodmacq, A. Schuhl, S. Pizzini, J. Vogel, P. Gambardella, *Nat. Mater.* **2010**, 9, 230.
[53] U. H. Pi, K. Won Kim, J. Y. Bae, S. C. Lee, Y. J. Cho, K. S. Kim, S. Seo, *Appl. Phys. Lett.* **2010**, 97, 162507.
[54] J. Kim, J. Sinha, M. Hayashi, M. Yamanouchi, S. Fukami, T. Suzuki, S. Mitani, H. Ohno, *Nat. Mater.* **2013**, 12, 240.
[55] R. Yoshimi, K. Yasuda, A. Tsukazaki, K. S. Takahashi, M. Kawasaki, Y. Tokura, *Sci Adv* **2018**, 4, eaat9989.
[56] K.-S. Lee, S.-W. Lee, B.-C. Min, K.-J. Lee, *Appl. Phys. Lett.* **2013**, 102, 112410.
[57] S. Fukami, T. Anekawa, C. Zhang, H. Ohno, *Nat. Nanotechnol.* **2016**, 11, 621.
[58] V. P. Amin, M. D. Stiles, *Phys. Rev. B* **2016**, 94, 104420.
[59] K. Dolui, B. K. Nikolić, *Phys. Rev. B* **2017**, 96, 220403.
[60] P. M. Haney, H.-W. Lee, K.-J. Lee, A. Manchon, M. D. Stiles, *Phys. Rev. B* **2013**, 87, 174411.

We demonstrate for the first time that the magnon current excited in an insulating antiferromagnetic layer by an electronic spin current in an epitaxial all-oxide heterostructure is effective for manipulating the perpendicular magnetization in a ferromagnetic layer. Furthermore, the critical current density to switch the magnetization is about one order of magnitude smaller than in conventional metallic systems.

Dongxing Zheng, Jin Lan, Bin Fang, Yan Li, Chen Liu, J. Omar Ledesma-Martin, Yan Wen, Peng Li, Chenhui Zhang, Yinchang Ma, Ziqiang Qiu, Kai Liu, Aurélien Manchon, and Xixiang Zhang*

High-efficiency magnon-mediated magnetization switching in all-oxide heterostructures with perpendicular magnetic anisotropy